



Airborne observations of the surface cloud radiative effect during different seasons over sea ice and open ocean in the Fram Strait

Sebastian Becker¹, André Ehrlich¹, Michael Schäfer¹, and Manfred Wendisch¹

¹Leipzig Institute for Meteorology (LIM), Leipzig University, Leipzig, Germany

Correspondence: Sebastian Becker (sebastian.becker@uni-leipzig.de)

Abstract. This study analyzes the surface cloud radiative effect (CRE) obtained during airborne observations of three campaigns in the Arctic north-west of Svalbard. The surface CRE quantifies the potential of clouds to modify the radiative energy budget of the surface and is calculated by combining broadband radiation measurements during low-level flight sections in mostly cloudy conditions with radiative transfer simulations of cloud-free conditions. The significance of surface albedo changes due to the presence of clouds is demonstrated and this effect is considered in the cloud-free simulations. The observations are discussed with respect to differences of the CRE between sea ice and open ocean surfaces, and between the seasonally different campaigns. The results indicate that the CRE depends on both cloud, illumination, surface, and thermodynamic properties. The solar and thermal-infrared (TIR) component of the CRE are analyzed separately and in combination. The inter-campaign differences of the solar CRE are dominated by the seasonal cycle of the solar zenith angle, with the largest cooling effect in summer. The lower surface albedo causes a larger solar cooling effect over open ocean than over sea ice, which amounts to -259 W m^{-2} (-108 W m^{-2}) and -65 W m^{-2} (-17 W m^{-2}), respectively, during summer (spring). Independent of campaign and surface type, the TIR CRE is only weakly variable and shows values around 75 W m^{-2} . In total, clouds show a cooling effect over open ocean during all campaigns. In contrast, clouds over sea ice exert a warming effect to the surface, which neutralizes during mid-summer. Given the seasonal cycle of the sea ice distribution, these results imply that clouds in the Fram Strait region cool the surface during the sea ice minimum in late summer, while they warm the surface during the sea ice maximum in spring.

1 Introduction

The enhanced warming and the rapid loss of sea ice are the most obvious signs of accelerated climate changes currently ongoing in the Arctic. Because these changes appear much faster compared to the rest of the globe, the term Arctic amplification was introduced (Serreze and Barry, 2011; Wendisch et al., 2017, 2022a). A multitude of atmospheric processes and feedback mechanisms contributes to this amplified transformation of the Arctic climate system. Clouds play a substantial, yet not fully understood, role in Arctic amplification by their involvement in several feedbacks. For example, the downward radiative energy fluxes in the thermal-infrared (TIR) spectral range ($\sim 4\text{--}100 \mu\text{m}$) are increased by clouds, which leads to a warmer surface and delayed refreezing, thinner sea ice, and faster melting (positive cloud–sea ice feedback, Morrison et al., 2019). At the same time, the increased fraction of liquid water in the clouds increases the cloud optical thickness and the reflection of solar radiation (\sim



0.3–4 μm) by the cloud (negative cloud optical thickness feedback, e. g., Zelinka et al., 2012; Ceppi et al., 2015). Furthermore, the indirect influence of clouds on other feedbacks is demonstrated by the reduction of the sea ice–albedo feedback in summer through increased cloud fraction or optical thickness (Kay et al., 2012; Choi et al., 2020). This multitude of partly opposing effects complicates the evaluation of the combined impact of clouds within the Arctic climate system and makes the sign
30 (warming or cooling) of the total cloud feedback uncertain (Forster et al., 2021).

In consequence, a realistic representation of the impact of clouds within the Arctic climate system in numerical weather and climate models appears crucial. In particular, the radiative energy budget (REB) of the surface and the atmosphere is largely determined by the presence and properties of clouds (Wendisch et al., 2022b). The REB is quantified by the difference of downward and upward irradiances, F^\downarrow and F^\uparrow , respectively; it is referred to as net irradiance F_{net} , with:

$$35 \quad F_{\text{net}} = F^\downarrow - F^\uparrow. \quad (1)$$

The cloud impact on the REB is quantified by the cloud radiative effect (CRE), which is also referred to as cloud radiative forcing (Ramanathan et al., 1989). It is derived from the difference of the net irradiances in cloudy ($F_{\text{net,cld}}$) and cloud-free ($F_{\text{net,cf}}$) atmospheric conditions:

$$\Delta F = F_{\text{net,cld}} - F_{\text{net,cf}}. \quad (2)$$

40 The CRE depends on both, microphysical (e. g., cloud phase; liquid water path, LWP; and effective radius, r_{eff}) and macrophysical (e. g., cloud fraction; cloud height) cloud properties, but also on the thermodynamic circumstances, the solar zenith angle (SZA), and the surface albedo (Shupe and Intrieri, 2004).

In contrast to the cooling effect of clouds on global average (Allan, 2011), long-term, ground-based observations at single locations around the Arctic identified an average warming effect of clouds at the surface, ranging from 3.5 W m^{-2} to 33 W m^{-2}
45 (Dong et al., 2010; Intrieri et al., 2002; Miller et al., 2015; Ebell et al., 2020). While the TIR warming effect dominates for the frequently occurring, relatively warm low-level clouds that are typically related to distinct temperature inversions, the solar cooling potential of the clouds is limited by the high surface albedo and SZA (during polar day) characteristic for the Arctic (e. g., Curry et al., 1996; Shupe and Intrieri, 2004). During summer, however, the relatively low SZA causes the solar cooling effect to dominate over the TIR warming effect (Ebell et al., 2020; Dong et al., 2010; Intrieri et al., 2002), which determines a
50 seasonal cycle of the CRE. Spatial differences of the environmental conditions among the measurement sites mainly cause the variability of the surface CRE found in the literature. For example, the average CRE observed during the Surface HEat Budget of the Arctic Ocean (SHEBA) drift experiment (Intrieri et al., 2002), or on the Greenland ice sheet (Summit, Miller et al., 2015), where the surface was covered by snow or ice all year round, is larger compared to the partly snow-free land surfaces at Barrow (Dong et al., 2010) or Ny-Ålesund (Ebell et al., 2020).

55 The comparison of the different CRE results is further hampered by the inconsistent consideration of the cloud impact on the thermodynamic profiles and on the surface albedo (Stapf et al., 2021a, 2020). Some studies applied the radiative-transfer approach, where the cloud-free state is simulated by only removing the cloud, neglecting adjustments of the thermodynamic profiles and the surface albedo between cloudy and cloud-free conditions (e. g., Intrieri et al., 2002). Others determined the



CRE from measurements only, which were obtained during cloudy and cloud-free conditions (e. g., Dong et al., 2010). This measurement-based approach accounts for the adjustment effects (Stapf et al., 2020). The resulting differences between the two approaches can be significant. Stapf et al. (2021a) demonstrated that, due to the decreased surface temperature, the TIR CRE obtained during SHEBA would be up to 25 W m^{-2} lower in autumn if the measurement-based approach was used. In summer, no significant differences were found. Since the temporal dependence of the thermodynamic adjustments to cloud dissipation complicates an accurate and continuous quantification of this effect (Walsh and Chapman, 1998; Wendisch et al., 2022b), differences between both approaches will remain and likely depend on cloud type, season, and surface conditions. In contrast, the conceptual differences resulting from the cloud-induced surface albedo change can be reduced for the radiative-transfer approach. For snow-covered surfaces, Stapf et al. (2020) applied an albedo parameterization to obtain the surface albedo in cloud-free conditions and found a doubling of the solar cooling effect in the Fram Strait at the beginning of the melting season when the retrieved albedo was used for the calculation of the cloud-free net irradiance.

The majority of previous CRE studies in the Arctic as well as the investigations of the cloud impact on the surface albedo and the CRE (Stapf et al., 2020) were conducted over sea ice or mostly snow-covered surfaces. Less efforts have been spent to study the CRE over open (ice-free) ocean (Kay et al., 2016), although this situation will become more dominant in the future Arctic. Over an open ocean, quite different characteristics of the mean CRE and the cloud impact on the surface albedo appear. However, measurements of the REB and the CRE are difficult to obtain over open ocean. Shipborne radiation measurements mostly consist of the downward irradiances only and rely on assumptions or complementary (e. g., satellite) measurements of surface albedo, near-surface air temperature, and surface emissivity to calculate the upward irradiances (Protat et al., 2017; Barrientos-Velasco et al., 2022). Polavarapu (1978) obtained the net irradiance from a combination of two pairs of radiometers, which were mounted at the left and right outsides of the ship's structure and shadowed at the half facing towards the ship. Kay and L'Ecuyer (2013) used satellite observations to derive the surface CRE and found an annual mean CRE similar to that from Ebell et al. (2020). However, both results included snow-covered and snow-free observations.

To characterize the CRE over the individual sea ice and open ocean surfaces in close proximity to each other, this study uses airborne measurements of broadband downward and upward irradiances combined with radiative transfer simulations. For this purpose, the data from three airborne campaigns performed during different seasons are analyzed. Section 2 introduces the measurements as well as the campaigns and their surface and meteorological characteristics. The radiative transfer simulations and the effect of the cloud-induced albedo change over open ocean are described in Sect. 3. The solar and the TIR CRE as well as their variability as a function of the surface type, and between the different campaigns are assessed in Sect. 4. Conclusions are given in Sect. 5

2 Observations

2.1 Airborne campaigns and instrumentation

To study atmospheric processes in the lower Arctic troposphere, airborne measurements of cloud, surface, and thermodynamic properties were performed during three seasonally distinct campaigns in the vicinity of Svalbard. The Airborne measurements



Table 1. Statistical overview of the analyzed campaigns.

Campaign	AFLUX	ACLOUD	MOSAIC-ACA
Period	19 March–11 April 2019	23 May–26 June 2017	30 August–13 September 2020
Aircraft	<i>Polar 5</i>	<i>Polar 5, Polar 6</i>	<i>Polar 5</i>
Total flight hours	67.5	178.5	44.3
Low-level flight hours	6.1	13.6	1.5
Observations over sea ice (%)	65	50	2
Observations over open ocean (%)	16	15	72
Observations over the MIZ (%)	19	35	26
Median SZA (°)	76	60	76

of radiative and turbulent FLUXes of energy and momentum in the Arctic boundary layer (AFLUX) campaign was conducted in early spring 2019 (Mech et al., 2022), while the Arctic CLOUD Observations Using airborne measurements during polar Day (ACLOUD) campaign was performed in late spring/early summer 2017 (Wendisch et al., 2019). Additionally, the Multidisciplinary drifting Observatory for the Study of Arctic Climate – Airborne observations in the Central Arctic (MOSAIC-ACA) campaign was conducted in late summer 2020 and accompanied the MOSAIC drift expedition with airborne measurements (Shupe et al., 2022). Table 1 lists the periods during which the campaigns were performed. During ACLOUD, the measurements were accomplished onboard the two research aircraft *Polar 5* and *Polar 6* from Alfred Wegener Institute, Helmholtz Centre for Polar and Marine Research (Wesche et al., 2016). During the other campaigns, only *Polar 5* was operated. The majority of the observations took place in the eastern Fram Strait north-west of Svalbard, the corresponding flight tracks are displayed in Fig. 1. Depending on the campaign, between 5 % and 20 % of the total flight time was dedicated to low-level flight sections, not exceeding a flight altitude of 250 m.

During the low-level sections, the broadband upward and downward irradiances were measured with a pair of downward- and upward-directed pyranometers (sensitive in the solar spectral range between 0.2–3.6 μm) and pyrgeometers (sensitive in the TIR range between 4.5–42 μm) at a frequency of 20 Hz. From these measurements, the net irradiance (Eq. 1) and the surface albedo (the ratio of solar upward and downward irradiances) in mostly cloudy conditions were derived. For aircraft attitudes exceeding 5° in roll and pitch angle, the irradiance data that are related to a horizontal reference plane, had to be discarded. This, and the exclusion of data due to severe icing of the instruments, led to a reduction of the low-level data set by 41 %, 63 %, and 44 % for AFLUX, ACLOUD, and MOSAIC-ACA, respectively. The remaining low-level flight time used for the analysis is given in Table 1. Additionally, the surface brightness temperature and the sea ice concentration were derived from measurements of a nadir-directed Kelvin infrared radiation thermometer (KT-19, sampling frequency of 20 Hz), and a three-channel digital camera equipped with a 180° fish-eye lens (sampling frequency of 1/6 Hz). The individual pixels of the radiance-calibrated images of the fish-eye camera were classified into the different surface types based on their reflection

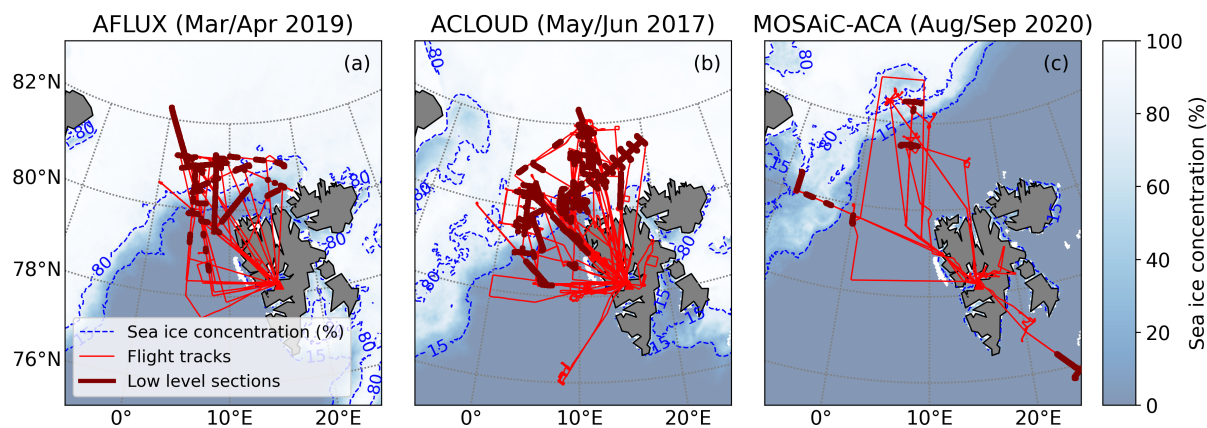


Figure 1. Flight tracks (red) and low-level sections (bold brown) performed during (a) AFLUX, (b) ACLOUD, and (c) MOSAiC-ACA. Each panel shows the mean sea ice concentration (derived from space-borne observations, Spreen et al., 2008) present during the respective campaign, the dashed blue lines indicate the 15 % and 80 % isolines of sea ice concentration that confine the MIZ according to the definition of Strong and Rigor (2013).

characteristics (Becker et al., 2022), in order to derive the cosine-weighted surface type fraction of each image. Based on
115 the transmissivity of the clouds, which is the fraction of the downward irradiances measured in mostly cloudy atmospheric
conditions and simulated for cloud-free conditions, an equivalent LWP was retrieved using the method of Stapf et al. (2020)
and assuming clouds with a droplet r_{eff} of $8 \mu\text{m}$. Despite the neglected cloud ice and the fixed r_{eff} in the retrieval, the equivalent
LWP provides a robust estimate of the optical thickness of the clouds. Regular profiles of temperature and relative humidity
were obtained using the in situ meteorological measurements during aircraft ascents and descents, sondes dropped from the
120 aircraft, and, for the higher atmosphere, radiosoundings launched at Ny-Ålesund. Measurements of profiles of the cloud liquid
water content (LWC) obtained from various in situ cloud probes were used to retrieve the cloud boundaries. Further details on
the aircraft instrumentation and data processing are provided by Ehrlich et al. (2019b) and Mech et al. (2022).

2.2 Sea ice situation during the campaigns

The different distributions of sea ice in the Fram Strait region during the three campaigns investigated in this paper are depicted
125 in Fig. 1 based on the space-borne observations of the sea ice concentration (Spreen et al., 2008). While the sea ice edge was
roughly located between $80\text{--}81^\circ \text{N}$ during AFLUX (Fig. 1a), it was situated slightly further south during ACLOUD (Fig. 1b).
During both campaigns, the region east of Svalbard was covered by almost closed sea ice. Since MOSAiC-ACA was performed
temporally close to the annual sea ice minimum, ice-free conditions were present east of the island and the sea ice edge in the
Fram Strait was mostly north of 82°N . It was reached by *Polar 5* only for a short flight section (Fig. 1c). Consequently,
130 more than half of the low-level observations during AFLUX and ACLOUD were performed over closed sea ice, while during
MOSAiC-ACA, the fraction of observations over sea ice amounts to only 2 % and strongly limits the statistical representation
of this situation. Instead, almost three quarters of the low-level observations were performed over open ocean during MOSAiC-

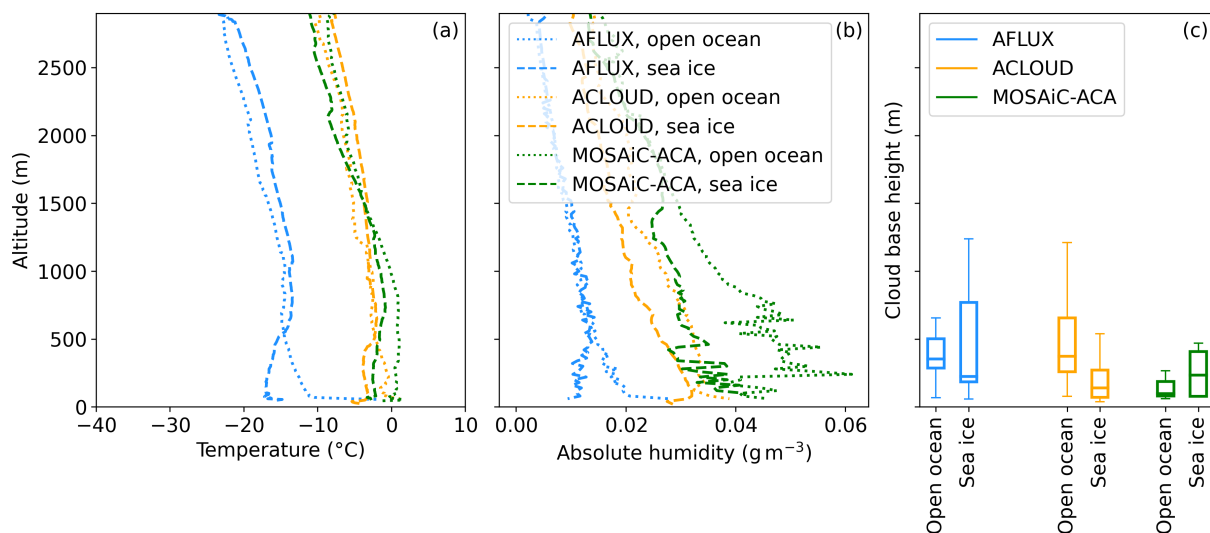


Figure 2. Mean profiles of (a) temperature, and (b) absolute humidity obtained during aircraft ascents and descents of the individual campaigns (colour-coded), separated for the different surface types (linestyle-coded). (c) Box-whisker plots of the cloud base height obtained from the in situ cloud probes (see text for details). The surface type separation is based on the space-borne observations of the sea ice concentration (Spren et al., 2008) and the surface type definition of Strong and Rigor (2013).

ACA compared to about 15 % during the other campaigns (Table 1). Note that for the low-level observations, the MIZ comprises all observations with f_{ice} between 0.05 and 0.95 and, thus, deviates from the MIZ definition of Strong and Rigor (2013), where f_{ice} is between 0.15 and 0.8. These modified thresholds are motivated by the strong impact of the surface type on the surface radiative properties, which significantly changes already for small fractions of sea ice or open ocean and requires a more rigorous separation of the MIZ (e. g., Becker et al., 2022).

2.3 Thermodynamic profiles and cloud base height

Mean profiles of various thermodynamic properties measured during the campaigns are shown in Figs. 2a and 2b. According to the time of the year, AFLUX showed significantly colder temperatures compared to the remaining campaigns (Fig. 2a). While the mean near-surface temperature over sea ice was -16°C during AFLUX, it was around -3°C during ACLOUD and MOSAiC-ACA. Although the temperature at the open ocean surface was close to the freezing point during all campaigns, it strongly decreased within the lowermost 80 m during AFLUX. Over sea ice, a surface-based temperature inversion was present during all campaigns, which was strongest during AFLUX. In contrast, temperature inversions were weak or absent over open ocean, with the least stable mean profile obtained for AFLUX. In higher altitudes, the mean profiles over sea ice and open ocean of the same campaign agreed well.

The emission and absorption by the atmospheric water vapour relevant for the surface TIR irradiances, depends on the absolute humidity (AH), which is shown in Fig. 2b. Due to the lower equilibrium pressure and the resulting lower concentration



of water vapour for colder temperatures, AFLUX showed the lowest AH. The differently shaped temperature profiles over sea
150 ice and open ocean below 500 m are imprinted in the mean AH profile. Despite the comparable temperature range, the AH was
significantly lower during ACLOUD than during MOSAiC-ACA, which is due to the lower relative humidity (RH, not shown).
Furthermore, the lower RH over sea ice reduced the AH compared to open ocean during ACLOUD. During MOSAiC-ACA,
both the higher temperature and the larger RH caused the increased AH over open ocean below 1500 m.

The surface TIR CRE largely depends on the cloud base temperature, which is determined by the location of the cloud within
155 the temperature profile. Figure 2c shows statistics of the cloud base height obtained from the in situ cloud probes. Clouds were
identified by a LWC threshold of 0.005 g cm^{-3} . During AFLUX, the median cloud base height over open ocean was 352 m.
Over sea ice, the median cloud base height was lower (223 m) but more variable. The typical cloud base temperature range is
estimated from the mean temperature (Fig. 2a) in the altitudes corresponding to the inter-quartile range (IQR) of the cloud base
height. For AFLUX, the cloud base temperature was in the range of $-14 \text{ }^\circ\text{C}$ over sea ice, and between $-13 \text{ }^\circ\text{C}$ and $-17 \text{ }^\circ\text{C}$
160 over open ocean. During ACLOUD, the median cloud base height of 372 m over open ocean was similar compared to AFLUX,
while clouds over sea ice were significantly lower (140 m). The resulting cloud base temperatures range around $-3\text{--}0 \text{ }^\circ\text{C}$ and
 $-3 \text{ }^\circ\text{C}$ over open ocean and sea ice, respectively. During MOSAiC-ACA, the median cloud base height over sea ice was 234 m,
while clouds over open ocean showed very low bases (97 m). The cloud base temperatures were about $0 \text{ }^\circ\text{C}$ and $-2 \text{ }^\circ\text{C}$ over
open ocean and sea ice, respectively. In general, the slightly colder cloud base temperatures over sea ice seem to result rather
165 from the colder low-level temperatures than from the different cloud base heights.

2.4 Cloud liquid water path

The statistical characteristics of the equivalent cloud LWP assembled during the campaigns are illustrated in Fig. 3 as a rough
measure for optical thickness. During AFLUX (Fig. 3a), clouds with an equivalent LWP below 10 g m^{-2} were most frequent
over sea ice, while the largest mode of equivalent LWP over open ocean occurs between 30 g m^{-2} and 50 g m^{-2} . The TIR CRE
170 is especially sensitive to the LWP of optically thin clouds below 30 g m^{-2} (e. g., Shupe and Intrieri, 2004; Ebell et al., 2020),
but almost constant for larger LWPs. Accordingly, this threshold was used to distinguish between thin and thick clouds, which
are analyzed separately. Corresponding to the PDFs, the median equivalent LWP of thin clouds is lower over sea ice than over
open ocean, with values of 15 g m^{-2} and 18 g m^{-2} , respectively (Fig. 3d). In contrast, the median of thick clouds is larger over
sea ice. However, thin clouds occurred more frequently over sea ice compared to open ocean (numbers in Fig. 3a).

175 The PDF of the equivalent LWP derived from ACLOUD measurements (Fig. 3b) reveals a similar distribution of thin clouds
over sea ice and open ocean. Both surface types showed similar median values for thin clouds (around 17 g m^{-2} , Fig. 3e). Over
open ocean, clouds with an equivalent LWP of $30\text{--}50 \text{ g m}^{-2}$ were most common, while larger LWPs were more frequent over
sea ice than over open ocean. Thus, the median equivalent LWP of thick clouds was larger over sea ice. The thin cloud fraction
was slightly lower over sea ice compared to open ocean. Compared to AFLUX, thin clouds occurred significantly less frequent
180 over both surface types.

During MOSAiC-ACA (Fig. 3c), the vast majority of the clouds over the sparsely sampled sea ice showed an extremely
low equivalent LWP. The median equivalent LWP of thin clouds was 7 g m^{-2} (Fig. 3f) and almost 90 % of the sampled clouds

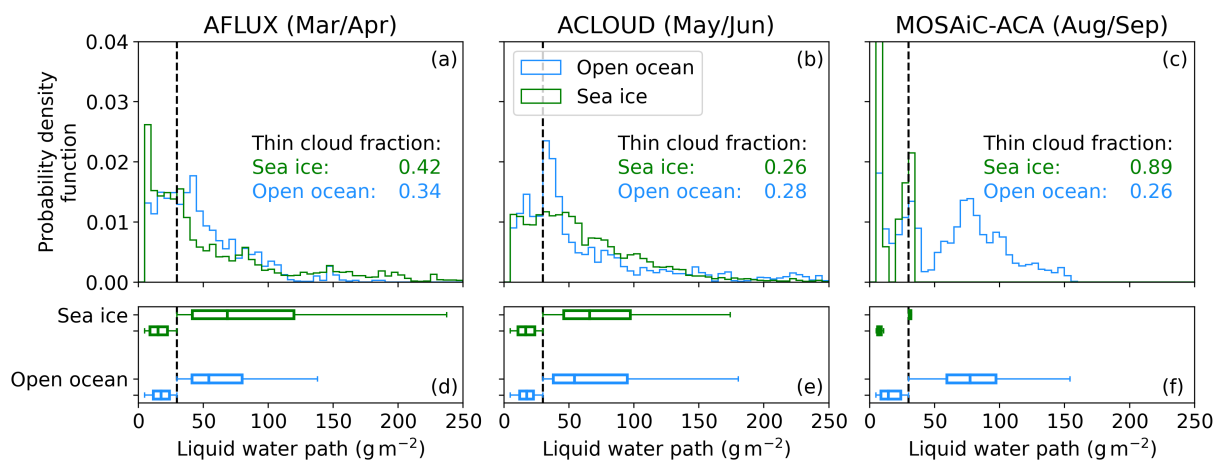


Figure 3. Probability density function of the equivalent LWP over sea ice and open ocean (colour-coded) for (a) AFLUX, (b) ACLOUD, and (c) MOSAiC-ACA. Only observations classified as cloudy (equivalent LWP $> 5 \text{ g m}^{-2}$) were considered. The vertical dashed lines located at 30 g m^{-2} indicate the threshold used for the separation of thin and thick clouds. The numbers in (a–c) represent the fraction of observations with thin clouds with respect to the total amount of cloudy observations. (d–f) Box-whisker plots of the equivalent LWP separating thin (left boxplots) and thick clouds (right boxplots).

were thin. In contrast, the equivalent LWP of clouds over open ocean showed a broader distribution with a strong mode of thick clouds. The thin cloud fraction over open ocean was similar to the one observed during ACLOUD. Compared to the other
185 campaigns, the median of the equivalent LWP of thin clouds over open ocean was slightly lower and amounted to 14 g m^{-2} .

3 Simulation of the net irradiance in assumed cloud-free conditions

3.1 Radiative transfer simulations

The net irradiance was measured in cloudy conditions (Sect. 2.1). To calculate the CRE (Eq. 2), the net irradiance in cloud-free conditions needs to be simulated. For this purpose, the one-dimensional radiative transfer solver DISORT is applied (Stamnes
190 et al., 1988), which is embedded in the library for radiative transfer *libRadtran* (Emde et al., 2016). The radiative transfer simulations were performed using the method proposed by Stapf et al. (2020). The atmospheric state was obtained from thermodynamic profiles measured during ascents or descents adjacent to the respective low level-section, which were topped by the temporally closest radiosounding. Aerosol properties were not considered in the simulations. The downward and upward irradiances in the TIR range were simulated using the thermodynamic profile and a surface emissivity of 0.99 for snow (Warren,
195 1982), which is similar for open ocean at least for the atmospheric window ($8\text{--}13 \mu\text{m}$) region (Konda et al., 1994). Beside the thermodynamic profile and the SZA, the simulation of the cloud-free irradiances in the solar spectral range requires to define the local surface albedo in cloud-free conditions, which is different from the surface albedo measured in cloudy conditions. From the simulated solar irradiances, the direct/diffuse fractions of the downward solar irradiance were obtained.



3.2 Impact of clouds on the surface albedo

200 3.2.1 Surface albedo over open ocean in cloud-free and cloudy conditions

While Stapf et al. (2020) analyzed the impact of clouds on the surface albedo of sea ice, the following analysis focuses on similar effects influencing the surface albedo of open ocean. The change of the broadband albedo due to the presence of clouds is a result of two effects: First, the changing illumination geometry (geometry effect), and, second, the changing spectral distribution of the downward solar irradiance (spectral weighting effect). In general, the broadband surface albedo α is given
205 by

$$\alpha = \frac{F_{\text{sol}}^{\uparrow}}{F_{\text{sol}}^{\downarrow}} = \frac{\int_{\text{sol}} F_{\lambda}^{\uparrow}(\lambda) d\lambda}{\int_{\text{sol}} F_{\lambda}^{\downarrow}(\lambda) d\lambda}. \quad (3)$$

The upward and downward solar irradiances, $F_{\text{sol}}^{\uparrow}$ and $F_{\text{sol}}^{\downarrow}$, are obtained by integrating the spectral upward and downward irradiances, F_{λ}^{\uparrow} and F_{λ}^{\downarrow} , over the wavelengths λ of the solar spectral range (indicated by \int_{sol}). To introduce the spectral albedo α_{λ} , F_{λ}^{\uparrow} is replaced by F_{λ}^{\downarrow} and α_{λ} :

$$210 \quad \alpha = \int_{\text{sol}} \alpha_{\lambda}(\lambda) \cdot \frac{F_{\lambda}^{\downarrow}(\lambda)}{\int_{\text{sol}} F_{\lambda}^{\downarrow}(\lambda) d\lambda} d\lambda. \quad (4)$$

Equation 4 shows that the broadband albedo represents a weighted average depending on the spectral albedo and the downward spectral irradiance, which serves as a weight function. While the spectral albedo changes due to the geometry effect, a change of the normalized weight function w , with

$$w = \frac{F_{\lambda}^{\downarrow}(\lambda)}{\int_{\text{sol}} F_{\lambda}^{\downarrow}(\lambda) d\lambda}, \quad (5)$$

215 describes the spectral weighting effect. Both effects are analyzed in the following.

The spectral surface albedo and the normalized weight function over open ocean were simulated with *libRadtran*, applying a parameterization of the directional reflection of open ocean surfaces with varying SZA and wind speed in 10 m altitude (Cox and Munk, 1954). To illustrate the effect of clouds on the surface albedo, simulations containing boundary layer clouds (400–600 m) with variable LWP and a fixed r_{eff} of 8 μm were performed.

220 The change of the spectral albedo due to different illumination geometries is shown in Fig. 4a. In cloud-free conditions, the spectral albedo is dominated by the reflection of the direct component of the incident spectral irradiance. Beside their different patterns, the spectral albedo is significantly larger for a SZA of 75°, which is representative for AFLUX and MOSAiC-ACA, compared to a SZA of 60°, representative for ALOUD. The almost constant spectral albedo above 1000 nm is 0.20 for 75°, but only 0.07 for 60°. This difference is due to the enhanced specular reflection at the air–water interface for larger incident
225 angles (i. e., SZA), according to Fresnel’s equations. In cloudy conditions (LWP of 80 g m^{-2}), the spectral surface albedo is modified by the diffuse illumination geometry and reveals slightly lower values compared to the cloud-free case with a SZA of 60°. The best agreement between the spectral albedo in cloudy and cloud-free conditions was found for a SZA of 52° (not

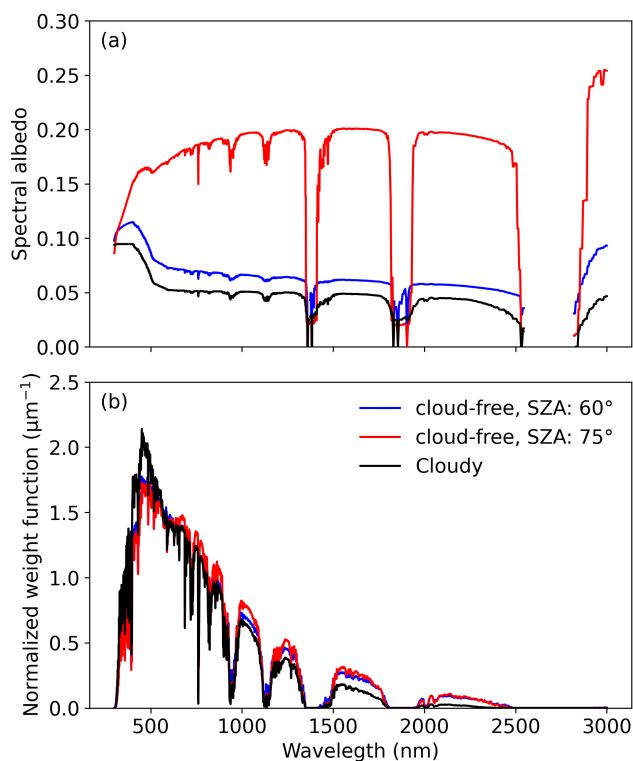


Figure 4. (a) Spectral surface albedo of open ocean for two different SZAs in cloud-free conditions, and for cloudy conditions (LWP of 80 g m^{-2} , independent of SZA). (b) Spectral normalized weight functions w for the same scenarios. The wind speed of 1 m s^{-1} represents a calm surface.

shown), which can be referred to as an effective incident zenith angle in cloudy conditions. Thus, the geometry effect causes a lower surface albedo in cloudy conditions compared to cloud-free conditions for SZAs typical for the Arctic, with a larger difference for larger SZAs. This difference decreases as the wind speed is increased, especially for large SZAs (Jin et al., 2004).

The broadband albedo is also affected by the spectral distribution of the incident irradiance (Eq. 4), which is described by w and can be modified by clouds. Spectra of w corresponding to the cases discussed above are illustrated in Fig. 4b. At visible wavelengths (e. g., 500 nm), w is larger in cloudy conditions compared to cloud-free conditions, while the situation is reversed in the near-infrared (NIR) range (e. g., 1600 nm) due to enhanced absorption by cloud particles. Consequently, the spectral albedo in the visible wavelength range, which is slightly higher compared to the albedo in the NIR range, contributes more strongly to the broadband albedo in cloudy conditions than it does in the cloud-free case. This spectral weighting partly counteracts the spectral albedo geometry effect on the broadband albedo.

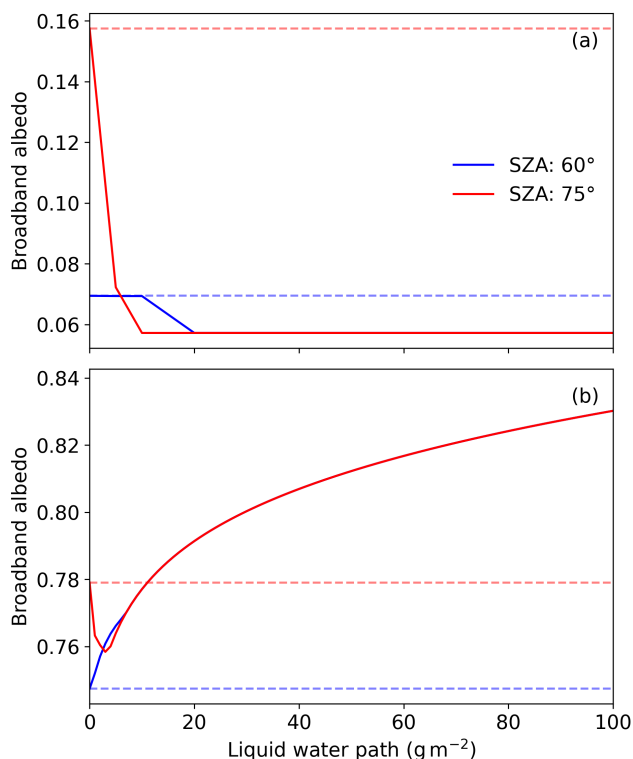


Figure 5. Broadband albedo of (a) open ocean, and (b) sea ice as a function of the cloud LWP for different SZAs. The open ocean albedo is based on the parameterization of Jin et al. (2011) with a 10 m wind speed of 1 m s^{-1} . The sea ice albedo is based on the parameterization of Gardner and Sharp (2010) with a SSA of $80 \text{ m}^2 \text{ kg}^{-1}$. The attenuated dashed lines represent the respective cloud-free surface albedos.

3.2.2 Parameterization of the open ocean and sea ice albedo in cloud-free conditions

To account for the cloud-induced change of the surface albedo in the calculation of the cloud-free net irradiance, parameterizations are used to retrieve the surface albedo in cloud-free conditions. The sea ice albedo is retrieved using the method described by Stapf et al. (2020), which is based on the parameterization of Gardner and Sharp (2010). This parameterization depends on the SZA, the equivalent cloud LWP, and the specific surface area (SSA) of snow, which is a measure for the snow grain size and was retrieved from the measured surface albedo. For open ocean, the parameterization of Jin et al. (2011) was used to obtain the surface albedo in cloud-free conditions. The required input include the SZA, the surface wind speed measured in flight altitude and scaled down to 10 m using the logarithmic wind profile with a roughness length of $2 \cdot 10^{-4} \text{ m}$ (offshore conditions), and the simulated fraction of diffuse incident radiation in cloud-free conditions (Sect. 3.1). For a mixture of open ocean and sea ice, the parameterized albedos of both surface types are linearly combined using the sea ice concentration.

Figure 5 illustrates the parameterized broadband albedo as a function of the LWP. The broadband open ocean albedo (Fig. 5a) decreases with increasing LWP, which indicates that the geometry effect dominates over the spectral weighting effect. This is due to the relatively low spectral differences of the spectral open ocean albedo (Fig. 4a). Similar to the spectral albedo, the

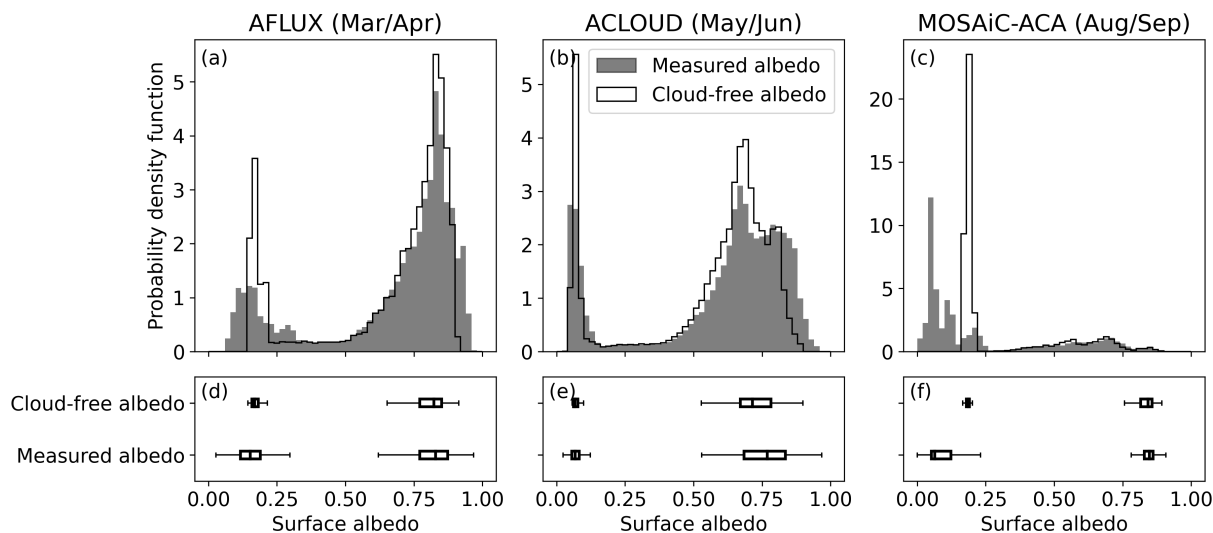


Figure 6. Probability density function of the surface albedos measured in mostly cloudy conditions (shadings) and retrieved for cloud-free conditions (lines) for (a) AFLUX, (b) ACLOUD, and (c) MOSAiC-ACA. (d–f) Box-whisker plots of the cloud-free and measured surface albedo separated for open ocean (left boxplots) and sea ice (right boxplots).

broadband open ocean albedo in diffuse conditions (LWPs larger than 20 g m^{-2}) is independent of the SZA and amounts to 0.06, while the albedo in cloud-free conditions increases for increasing SZA. Thus, the cloud-free albedo is only slightly larger than the diffuse albedo for a SZA of 60° , but reaches 0.16 for a SZA of 75° . For larger wind speeds, the difference between the cloudy and cloud-free albedos decreases (not shown).

255 In contrast to open ocean, the spectral albedo of snow-covered sea ice shows large discrepancies, with high values in the visible and low values in the NIR spectral range (e. g., Stapf et al., 2020, their Fig. 3). Thus, the spectral weighting effect becomes more dominant and leads to an increase of the broadband albedo with increasing LWP (Fig. 5b). While this is true for the entire LWP range for a SZA of 60° , a slight albedo decrease is observed for the lowest LWPs and a SZA of 75° . The cloud-free albedo is 0.75 and 0.78 for SZAs of 60° and 75° , respectively. Similar to open ocean, the surface albedo of sea ice
 260 does not differ with SZA in diffuse conditions. Consequently, the albedo differences between cloudy and cloud-free conditions are larger for lower SZAs within the typical LWP range.

To retrieve the cloud-free surface albedo from the mostly cloudy albedo measurements performed during the low-level sections, the surface albedo parameterizations were applied to the measurements of the three campaigns. Figure 6 illustrates the effect of the cloud-induced albedo change by comparing the frequency distributions of the measured (cloudy) and retrieved
 265 (cloud-free) surface albedos. The left and the right mode of all distributions correspond to the open ocean and sea ice surfaces, respectively. Compared to the measured albedo, the distribution of the cloud-free albedo is narrowed over open ocean during AFLUX (Figs. 6a, 6d). Although a notably higher open ocean albedo would be expected in cloud-free conditions for SZAs present during AFLUX (Fig. 5a), the cloudy and cloud-free median albedo values of 0.15 and 0.17, respectively, did not differ



significantly. This is probably due to the frequently occurring sea smoke between the aircraft and the ocean surface, which
270 artificially increased the measured albedo compared to the expected values (Fig. 5a). For the snow-covered sea ice, the median
values of 0.83 and 0.82 indicate only small differences between the cloudy and cloud-free albedos, which is in accordance with
Fig. 5b for the typical SZA range during AFLUX. Similarly, no significant difference between cloudy and cloud-free albedo
of open ocean could be observed during ACLOUD (Figs. 6b, 6e). However, as suggested by Fig. 5b, a significant albedo shift
275 over sea ice is obvious for ACLOUD, where the median of the surface albedo decreased from 0.77 in the observed cloudy
conditions to 0.71 for the retrieved cloud-free albedo. In general, the observations during ACLOUD are characterized by a
lower sea ice albedo compared to AFLUX, which is due to the onset of the melting season. Despite the similar SZA range,
the cloud-induced change of the open ocean albedo showed different effects for AFLUX and MOSAiC-ACA. The median of
the measured cloudy albedo was only 0.06 during the latter (Figs. 6c, 6f). However, the median cloud-free albedo of 0.19 was
similar to the value retrieved for AFLUX. The rarely sampled sea ice during MOSAiC-ACA is only expressed by the rightmost,
280 very small mode. Similar to AFLUX, the sea ice albedo did not change significantly between cloudy and cloud-free conditions.
The mode located roughly between 0.25 and 0.75 represents observations over the MIZ.

4 Cloud radiative effect

4.1 Solar cloud radiative effect

The variability of the solar CRE at the surface during the three campaigns is assessed by analyzing their different mode
285 structures. Since the solar CRE strongly depends on the surface albedo, Fig. 7 shows the frequency distributions of the solar
CRE as a function of the measured surface albedo. To quantify the impact of the cloud-induced albedo change on the solar CRE,
two distributions are presented for each campaign. While the surface albedo change is neglected in Figs. 7a–7c, Figs. 7d–7f
show the solar CRE corrected for this effect. For AFLUX and ACLOUD, the distributions of Fig. 7 reveal four distinct modes
(indicated by the numbers 1–4). The modes 1 and 2 are located around or slightly above 0 W m^{-2} and reflect mainly cloud-
290 free conditions, while the remaining modes (modes 3 and 4) indicate the cooling effect of clouds in the solar spectral range.
Through their distinct surface albedos, the solar CREs over open ocean (mode 3) and sea ice (mode 4) surfaces are clearly
distinct. During MOSAiC-ACA (Figs. 7d, 7f), thin or broken clouds (mode 5) and frequent observations over the MIZ in
cloudy conditions (mode 6) altered the mode structure.

The comparison of the two distributions per campaign exposes the shift of several modes due to the cloud-induced albedo
295 change. For AFLUX (Figs. 7a, 7d), only minor changes can be observed, which is in accordance with the similar distributions
of measured and retrieved (cloud-free) surface albedo (Fig. 6a). The albedo change increased (reduced) the median solar CRE
over open ocean (sea ice) by 4 W m^{-2} . The artificial absence of a larger CRE increase over open ocean is due to the sea
smoke and the resulting too high measured surface albedo discussed in Sect. 3.2.2. The actual change of the solar CRE remains
unclear. As discussed by Stapf et al. (2020), the increased albedo of sea ice in cloudy conditions caused a significant shift of
300 mode 4 during ACLOUD (Figs. 7b, 7e) and almost doubled the median of the uncorrected solar cooling effect of -33 W m^{-2} .
In contrast, the solar CRE over open ocean was hardly affected. During MOSAiC-ACA, the reduction of the solar cooling effect

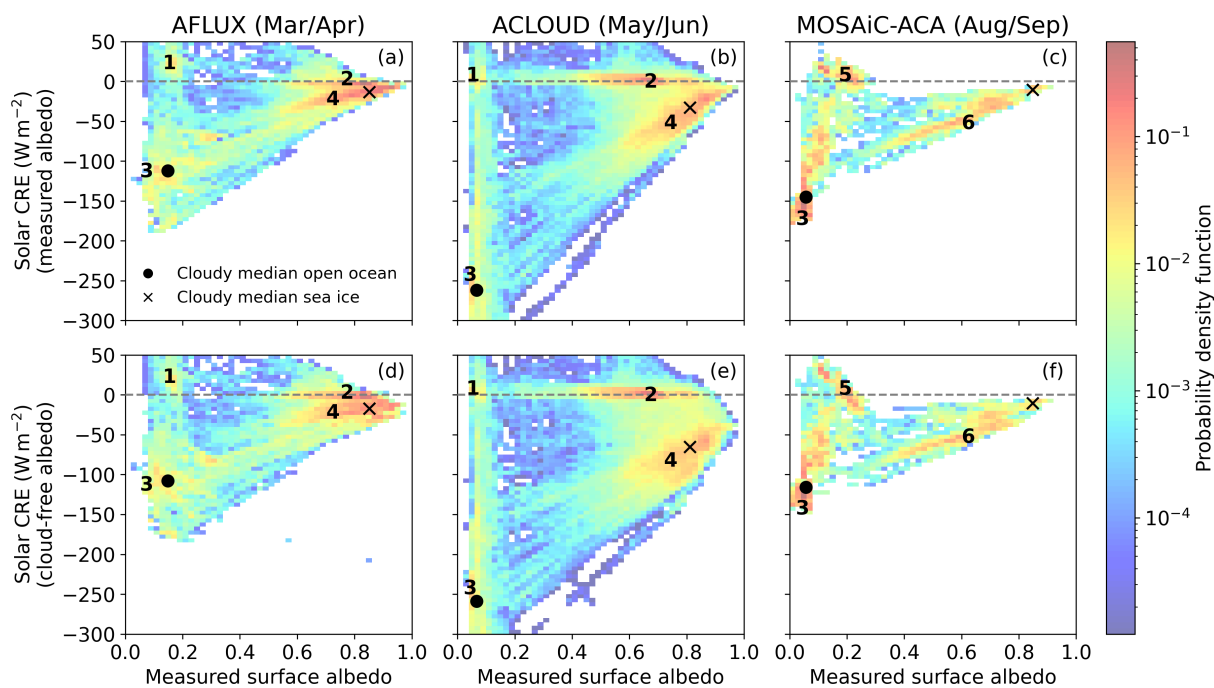


Figure 7. Two-dimensional probability density function of the solar CRE and the measured (mostly cloudy) surface albedo (as an indicator for the surface type) for AFLUX (a,d), ACLOUD (b,e), and MOSAiC-ACA (c,f). The upper row (a–c) shows the distributions of the solar CRE neglecting the cloud-induced change of the surface albedo, while this effect is included in the lower row (d–f). The horizontal dashed lines mark a CRE of 0 W m^{-2} . The symbols represent the cloudy (equivalent LWP $> 5 \text{ g m}^{-2}$) median CREs and measured surface albedos over the different surface types.

due to the increased open ocean albedo in cloud-free conditions (Fig. 6c) is expressed by the shift of mode 3 (Figs. 7c, 7f). The median of the uncorrected solar CRE (-145 W m^{-2}) was increased by 29 W m^{-2} . The sea ice-dominated MIZ (mode 6) is not affected by the albedo change, because the slight increase of the sea ice albedo and the more significant decrease of the open ocean albedo towards cloud-free conditions cancel.

Using the solar CRE accounting for the cloud-induced albedo change (Figs. 7d–7f), the features of the individual distributions and the differences among them are discussed in the following. Interestingly, the cloud-free open ocean mode (mode 1) of the AFLUX distribution (Fig. 7d) shows a positive CRE, with a median of 20 W m^{-2} for an equivalent LWP of less than 5 g m^{-2} . Probably, broken clouds, which in most cases do not shade the Sun, caused an enhanced solar downward irradiance compared to the cloud-free radiative transfer simulations, by scattering additional solar radiation towards the surface (Schade et al., 2007). This might have led to a retrieved equivalent LWP, which is low and, thus, almost indistinguishable from cloud-free conditions. Due to the high surface albedo of sea ice (larger than 0.6), the magnitude of the solar CRE was small over this surface type (mode 4, median of -17 W m^{-2}) and could be hardly distinguished from the absent CRE in cloud-free conditions



(mode 2), especially for very bright scenes. In contrast, the low open ocean albedo enabled a much larger solar cooling effect
315 of the clouds (mode 3) with a median CRE of -108 W m^{-2} .

The CRE distribution of ACLOUD (Fig. 7e) is shaped more clearly compared to AFLUX due to the better statistics of the
data. The solar CRE over open ocean and sea ice (modes 3 and 4) reveals median values of -259 W m^{-2} and -65 W m^{-2} ,
respectively, which indicates a significantly larger magnitude of the solar cooling effect compared to AFLUX. Although the
lower surface albedo contributed to the larger cooling effect during ACLOUD, the major contribution to the solar CRE differ-
320 ences between the two campaigns resulted from the different solar illumination as a consequence of the clearly distinct SZA
ranges (Table 1). Note that the SZA exhibits not only an annual, but also a daily cycle. However, since most of the flights were
conducted around solar noon, the SZA variability within one campaign was small.

The observations from MOSAiC-ACA reveal a large variability and a relatively blurry mode structure (Fig. 7f), which
is due to the much less significant statistics compared to the other campaigns (see Table 1). Modes 1 and 2 are missing in
325 the distribution, since cloud-free conditions were not sampled during MOSAiC-ACA. Instead of mode 1, mode 5 represents
broken or very thin clouds over open ocean. Similar to AFLUX, this mode peaks at positive CRE values due to the broken cloud
effect. However, in contrast to AFLUX, also negative CRE values were observed, probably resulting from rather overcast thin
cloud conditions. Due to the similar Sun elevation (Table 1), the median of the CRE over open ocean (-116 W m^{-2} , mode 3)
was similar compared to AFLUX. In contrast to the other campaigns, the rare observations over homogeneous sea ice during
330 MOSAiC-ACA are not reflected in an own mode. These observations are rather included in the cloudy MIZ mode (mode 6),
which expands to albedo values of down to 0.4.

The analysis of the solar CRE indicated a significant variability of the solar CRE between the campaigns and the underlying
surface types. In accordance with previous studies (e. g., Intrieri et al., 2002; Miller et al., 2015), the solar CRE between the
campaigns mostly varied due to the seasonally changing SZA, with an increasing cooling effect for a decreasing SZA. The
335 differences between open ocean and sea ice are a result of their distinct surface albedos. The impact of clouds on the surface
albedo affects the solar CRE differently, depending on surface type and SZA. While the albedo in cloudy conditions and the
solar cooling effect of clouds over sea ice are mostly increased for relatively low Arctic SZAs, larger SZAs rather reduce
the cooling effect over open ocean. Given the seasonality of the sea ice extent in the Fram Strait region (Fig. 1), this effect
rather enhances the cooling effect during early summer and reduces it during late summer. The resulting convergence of the
340 affected cloudy modes during ACLOUD and MOSAiC-ACA (Fig. 7) suggests a reduced amplitude of the seasonal CRE cycle
considering the cloud-induced albedo modifications.

4.2 Thermal-infrared cloud radiative effect

The TIR CRE is determined by a complex interplay of the environmental thermodynamics, and the cloud macrophysical and
microphysical properties. The frequency distributions of the TIR CRE for all three campaigns are depicted in Fig. 8, separated
345 for sea ice and open ocean. Independent of the underlying surface type, the distributions of the TIR CRE during AFLUX
(Figs. 8a, 8d) and ACLOUD (Figs. 8b, 8e) reveal two distinct modes. Similar to the solar CRE, the mode located around
 0 W m^{-2} represents cloud-free conditions, while the second mode clearly indicates the warming effect of the clouds in the TIR

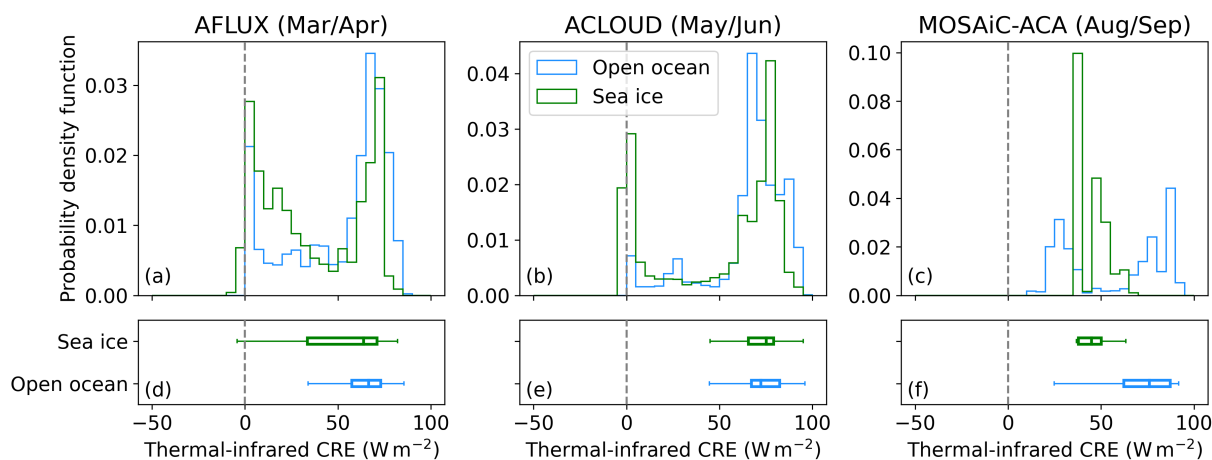


Figure 8. Probability density function of the TIR CRE for (a) AFLUX, (b) ACLOUD, and (c) MOSAiC-ACA, separated for sea ice and open ocean (colour-coded). (d–f) Box-whisker plots of the TIR CRE only considering cloudy observations (equivalent LWP $> 5 \text{ g m}^{-2}$). The vertical dashed lines mark a CRE of 0 W m^{-2} .

range. In contrast to the solar CRE, the order of magnitude of the TIR CRE range does not differ between the surface types because the surface temperature does not affect the CRE. Differences result only from the influence of the surface on the cloud and thermodynamic properties.

The median TIR CRE observed in cloudy conditions during AFLUX was 67 W m^{-2} over open ocean and 64 W m^{-2} over sea ice. The slightly lower value for the latter was caused by the enhanced frequency of observations with relatively low TIR CRE ($< 30 \text{ W m}^{-2}$), which might be linked to the larger fraction of thin clouds (Fig. 3a) or to the slightly lower cloud base temperature (Fig. 2) over sea ice. For AFLUX, a cloud base temperature change of 1 K results in a change of the TIR CRE in the order of 4 W m^{-2} , which is approximately the difference between the median TIR CREs over sea ice and open ocean.

During ACLOUD (Figs. 8b, 8e), cloud-free conditions were significantly less frequent over open ocean than over sea ice. Instead, the distribution of open ocean reveals an additional small mode around 25 W m^{-2} . The TIR CRE in cloudy conditions did not differ significantly between the surface types with median values ranging between 72 W m^{-2} over open ocean and 75 W m^{-2} over sea ice. The slightly larger TIR CRE over sea ice cannot be explained by the cloud base temperature (Fig. 2), which showed lower values over sea ice. Likely, the more frequent occurrence of thick clouds (Fig. 3b) caused this tendency. Also compared to AFLUX, the thicker clouds during ACLOUD are likely the reason for the larger surface TIR CRE, since the increased absolute humidity counteracts the effect of the higher cloud base temperature during ACLOUD (Cox et al., 2015). Except the additional small mode for open ocean, the cloud-free and cloudy modes are more clearly separated during ACLOUD compared to AFLUX.

Similar to the solar CRE, the low amount of data obtained during MOSAiC-ACA results in a less significant mode structure (Figs. 8e, 8f). Only in the distribution of open ocean, two distinct modes are visible. Due to the lack of cloud-free observations, the mode with the smallest CRE is located around 25 W m^{-2} and represents the broken cloud conditions. However,

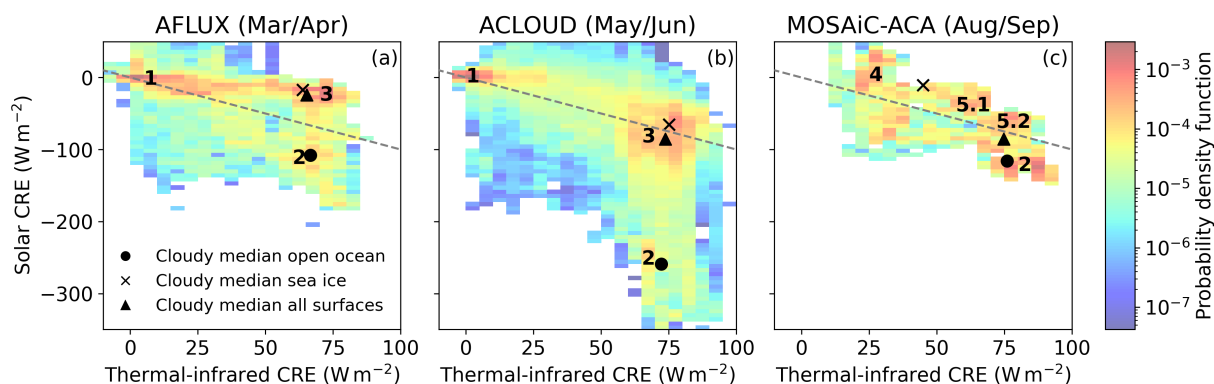


Figure 9. Two-dimensional probability density function of the solar and the TIR CRE for (a) AFLUX, (b) ACLOUD, and (c) MOSAiC-ACA. The diagonal dashed lines represent the 0 W m^{-2} isocline of the total (i. e., the sum of the solar and TIR) CRE. The symbols represent the cloudy (equivalent LWP $> 5 \text{ g m}^{-2}$) median CREs over the different surface types.

these observations mostly coincide with an equivalent LWP of less than 5 g m^{-2} and do not significantly contribute to the cloudy median CRE of 75 W m^{-2} over open ocean. This median value is similar to the median TIR CRE obtained during
 370 ACLOUD, which is probably due to the similar frequency of thick clouds (Fig. 3). Over sea ice, a significantly lower TIR CRE was observed during MOSAiC-ACA (45 W m^{-2}), which results from the limited sampling statistics. Nevertheless, this is in agreement with the lower observed cloud base temperature (Fig. 2) and the significantly thinner clouds (Fig. 3c).

4.3 Total cloud radiative effect

The previous analysis showed that the variability of the CRE between the campaigns and the surface types is significantly lower
 375 in the TIR than in the solar spectral range. Thus, the variability of the solar CRE is the major driver of the variability of the total (i. e., the sum of solar and TIR) CRE. Depending on whether the solar cooling or the TIR warming effect dominates, the total CRE determines whether a cloud has a cooling or a warming effect on the surface. Figure 9 illustrates two-dimensional frequency distributions combining the solar and the TIR effects to assess the total CRE.

All modes visible in Fig. 9 can be attributed to the modes discussed in Figs. 7 and 8. In the distributions of AFLUX (Fig. 9a) and ACLOUD (Fig. 9b), mode 1 is clustered around 0 W m^{-2} for both solar and TIR CRE and combines the cloud-free
 380 observations over open ocean and sea ice. The clearly distinct solar cooling effect over the different surface types (Fig. 7) separates the cloudy modes over open ocean (mode 2, larger solar cooling effect) and sea ice (mode 3), while the TIR warming effect is similar.

Over open ocean (mode 2), clouds of sufficient LWP showed a total cooling effect (values below the dashed line in Fig. 9) during all campaigns. However, the magnitudes of the CRE differed significantly as quantified by the median values of
 385 -48 W m^{-2} , -185 W m^{-2} , and -36 W m^{-2} during AFLUX, ACLOUD, and MOSAiC-ACA, respectively. Due to the lower SZA during ACLOUD, the solar cooling effect dominated the total CRE. Over sea ice, the TIR warming effect was dominant



over the solar cooling effect during AFLUX, resulting in a median total warming of 42 W m^{-2} . During ACLOUD, however, the solar cooling roughly compensated the TIR warming, leading to a small median total CRE of 7 W m^{-2} .

390 During AFLUX, a significant amount of observations ranges in a transition between modes 1 and 3. These data correspond to the observations over sea ice with low TIR CRE that were already discussed in Fig. 8a. The clouds during these situations were rather thin with a median equivalent LWP of 19 g m^{-2} compared to 54 g m^{-2} for the observations forming the cloudy sea ice mode (mode 3). The almost absent solar cooling in combination with a TIR warming leads to the total warming effect of these thin clouds often discussed in literature (e. g., Miller et al., 2015), which under certain circumstances can induce ice
395 melting (Bennartz et al., 2013).

Again, the sparse statistics during MOSAiC-ACA need to be interpreted with caution and represent only a subsample of possible cloud conditions (Fig. 9c). Instead of the cloud-free mode (mode 1) observed for the other campaigns, mode 4 represents the broken clouds that produced only a slightly positive solar, but a significantly positive TIR CRE with median values of 7 W m^{-2} and 26 W m^{-2} , respectively. The resulting positive total CRE underlines that the warming effect of broken clouds
400 can be observed also over open ocean. Modes 5.1 and 5.2 reveal a cloud warming effect over the MIZ, while a separate sea ice mode is missing.

For the regional average CRE, the sea ice concentration within the area of observations is most relevant. While the sea ice situation in the Fram Strait north-west of Svalbard was similar during AFLUX and ACLOUD (Figs. 1a and 1b), the sea ice edge was located significantly further north during MOSAiC-ACA (Fig. 1c) and the MIZ was broader. This also affected the
405 fraction of observations obtained for each of the surface types and determined the strength of the different modes in Fig. 9. As a proxy for the entire Fram Strait, the median of the total CRE observed in cloudy conditions during one single campaign was calculated regardless of surface type (triangles in Fig. 9). For MOSAiC-ACA, this median CRE of -27 W m^{-2} was close to the median for open ocean due to the dominance of this surface type. During AFLUX, a positive median CRE of 25 W m^{-2} , and during ACLOUD, a negative median CRE of -16 W m^{-2} was observed, both ranging close to median values of sea ice.
410 Given the different SZA ranges during both campaigns, this indicates that clouds over the Fram Strait showed a warming effect on the surface during AFLUX (spring) and an almost neutral to slightly negative CRE during ACLOUD (early summer). MOSAiC-ACA revealed a similar median of the total CRE compared to AFLUX for the individual surface types. However, the dominant open ocean surfaces during MOSAiC-ACA caused the clouds to have an average cooling effect during late summer.

5 Conclusions

415 To compare the warming or cooling effects of clouds over sea ice and open ocean during different times of the year, the surface CRE was evaluated from observations performed during three campaigns in the Fram Strait north-west of Svalbard. The campaigns AFLUX, ACLOUD, and MOSAiC-ACA were characterized by significantly different sea ice coverages and thermodynamic states during spring, early summer, and late summer, respectively. The CRE was calculated from a combination of airborne broadband radiation measurements and radiative transfer simulations. While the net irradiance in cloudy conditions
420 was measured during low-level flight sections, the corresponding cloud-free net irradiance was simulated and accounted for



changes of the surface albedo between cloudy and cloud-free conditions (Stapf et al., 2020). This was done by retrieving the cloud-free surface albedo from parameterizations for sea ice and open ocean surfaces. The radiative impact of clouds on the surface albedo differed between the surface types and was not uniform among the different campaigns.

425 The solar and total CRE were affected distinctly by these cloud-induced differences of the surface albedo, mainly depending on the SZA. The consideration of this effect almost doubled the solar cooling effect over sea ice during ACLOUD, as already discussed by Stapf et al. (2020). In contrast, the larger SZAs present during the other campaigns suppressed similar changes of the CRE. However, over open ocean, the impact of the cloud-induced albedo change increases with increasing SZA. Thus, the solar cooling effect over open ocean was reduced by about 20 % during MOSAiC-ACA, while ACLOUD was not affected. During AFLUX, the albedo change was masked by the presence of sea smoke.

430 The solar CRE strongly varied between sea ice and open ocean surfaces as well as among the campaigns. While the low surface albedo caused a large solar cooling effect over open ocean, the cooling effect over sea ice was rather weak and partly not distinguishable from cloud-free conditions. This weak cooling was often supported by the presence of thin clouds. Due to the lower SZA, the solar CRE showed a significantly larger cooling during ACLOUD compared to the other campaigns.

435 The variability of the TIR CRE results from a complex interplay between changing thermodynamic and cloud properties. In contrast to the solar CRE, the TIR CRE varied only weakly between the surface types and the campaigns and mostly showed median values between 64 W m^{-2} and 76 W m^{-2} . Compared to the other campaigns, a lower TIR CRE was found during AFLUX, which was caused by the enhanced frequency of optically thin clouds.

440 The variability of the total CRE is driven by the solar CRE. A total cooling effect, dominated by the solar cooling effect, was found over open ocean during all campaigns. This cooling effect was largest during ACLOUD (-185 W m^{-2}) compared to the other two campaigns (around -40 W m^{-2}). Over sea ice and the MIZ, the TIR warming effect clearly dominated during AFLUX (42 W m^{-2}) and MOSAiC-ACA (22 W m^{-2}), while the solar cooling and the TIR warming effect roughly compensated during ACLOUD. Broken and optically thin clouds showed a total warming effect, independent of the underlying surface. This is due to their almost neutral to slightly positive solar CRE and their significantly positive TIR CRE. In addition to the SZA, the total CRE not separated for the surface types differs between the campaigns due to the seasonally different sea ice 445 distributions. For each campaign, the sea ice distribution in the Fram Strait region is imprinted in the fraction of observations over the respective surface types. The high fraction of observations over sea ice during AFLUX and ACLOUD implies a warming and almost neutral effect of clouds in the Fram Strait during spring and early summer, respectively. In contrast, the frequent observations over open ocean during MOSAiC-ACA cause a cooling effect of clouds in the Fram Strait during late summer.

450 The short low-level flight segments during the campaigns are not necessarily representative for an entire season from a climatological point of view. However, various CRE differences between the campaigns could be attributed to their seasonality. Although observations of annual cycles of the CRE over sea ice are available (e. g., SHEBA, MOSAiC), the lack of long-term observations over open ocean complicates a robust characterization of the CRE. This especially holds since ice-free conditions will likely become more dominant in the future Arctic. However, the predominant cooling effect of clouds over open ocean will 455 lead to a negative contribution to further warming in the Arctic. This study and the published datasets of the CRE in the Fram



Strait (Stapf et al., 2021c; ?) provided a basis for further investigations of cloud-related processes and feedback mechanisms in numerical models.

Data availability. All data analyzed in this manuscript are published on the PANGAEA database. The broadband irradiance and KT19 data can be found at Stapf et al. (2019, <https://doi.pangaea.de/10.1594/PANGAEA.900442>, ACLOUD), Stapf et al. (2021b, <https://doi.pangaea.de/10.1594/PANGAEA.932020>, AFLUX), and Becker et al. (2021b, <https://doi.pangaea.de/10.1594/PANGAEA.936232>, MOSAiC-ACA). The meteorological measurements (temperature, RH, wind speed) during the flights were published by Hartmann et al. (2019, <https://doi.pangaea.de/10.1594/PANGAEA.902849>, ACLOUD), Lüpkes et al. (2022, <https://doi.pangaea.de/10.1594/PANGAEA.945844>, AFLUX), and Hartmann et al. (2022, <https://doi.pangaea.de/10.1594/PANGAEA.947787>, MOSAiC-ACA). Dropsonde measurements were provided by Ehrlich et al. (2019a, <https://doi.pangaea.de/10.1594/PANGAEA.900204>, ACLOUD), Becker et al. (2020, <https://doi.pangaea.de/10.1594/PANGAEA.921996>, AFLUX), and Becker et al. (2021a, <https://doi.pangaea.de/10.1594/PANGAEA.933581>, MOSAiC-ACA), while the radiosounding are available at Maturilli (2020, <https://doi.pangaea.de/10.1594/PANGAEA.914973>). The microphysical cloud properties obtained from the in situ cloud probes can be found at Dupuy et al. (2019, <https://doi.pangaea.de/10.1594/PANGAEA.899074>, ACLOUD), Moser and Voigt (2022, <https://doi.pangaea.de/10.1594/PANGAEA.940564>, AFLUX), and Moser et al. (2022, <https://doi.pangaea.de/10.1594/PANGAEA.940557>, MOSAiC-ACA). Datasets containing the retrieved sea ice fraction, equivalent LWP, cloud-free albedo, and CRE were published by Stapf et al. (2021c, <https://doi.pangaea.de/10.1594/PANGAEA.932010>, ACLOUD and AFLUX) and ?, ..., MOSAiC-ACA.

Author contributions. All authors contributed to the discussion of the results and the editing of the article. SB drafted the article, analyzed the data, and performed the ocean albedo analysis. MW and AE designed the experimental basis of this study.

Competing interests. The authors declare that they have no conflict of interest.

Acknowledgements. We gratefully acknowledge the funding by the Deutsche Forschungsgemeinschaft (DFG, German Research Foundation) – Projektnummer 268020496 – TRR 172, within the Transregional Collaborative Research Center “Arctic Amplification: Climate Relevant Atmospheric and SurfaCe Processes, and Feedback Mechanisms (AC)³. This work was carried out and data used in this article were produced as part of the international Multidisciplinary drifting Observatory for the Study of Arctic Climate (MOSAiC) with the tag MOSAiC20192020 during the Airborne observations in the Central Arctic (MOSAiC-ACA, P5-221_MOSAiC_ACA_2020). We thank AWI logistics department, the crews of the research aircraft Polar 5 and 6 and all persons involved in the expedition of the Research Vessel Polarstern during MOSAiC (AWI_PS122_00) as listed in Nixdorf et al. (2021). This work was funded by the Open Access Publishing Fund of Leipzig University supported by the DFG within the program Open Access Publication Funding.



References

- Allan, R. P.: Combining satellite data and models to estimate cloud radiative effect at the surface and in the atmosphere, *Meteorol. Appl.*, 18, 324–333, <https://doi.org/10.1002/met.285>, 2011.
- Barrientos-Velasco, C., Deneke, H., Hünerbein, A., Griesche, H. J., Seifert, P., and Macke, A.: Radiative closure and cloud effects on the radiation budget based on satellite and shipborne observations during the Arctic summer research cruise, PS106, *Atmos. Chem. Phys.*, 22, 9313–9348, <https://doi.org/10.5194/acp-22-9313-2022>, 2022.
- Becker, S., Ehrlich, A., Stapf, J., Lüpkes, C., Mech, M., Crewell, S., and Wendisch, M.: Meteorological measurements by dropsondes released from POLAR 5 during AFLUX 2019, PANGAEA, <https://doi.org/10.1594/PANGAEA.921996>, 2020.
- Becker, S., Ehrlich, A., Mech, M., Lüpkes, C., and Wendisch, M.: Meteorological measurements by dropsondes released from POLAR 5 during MOSAiC-ACA 2020, PANGAEA, <https://doi.org/10.1594/PANGAEA.933581>, 2021a.
- Becker, S., Stapf, J., Ehrlich, A., and Wendisch, M.: Aircraft measurements of broadband irradiance during the MOSAiC-ACA campaign in 2020, PANGAEA, <https://doi.org/10.1594/PANGAEA.936232>, 2021b.
- Becker, S., Ehrlich, A., Jäkel, E., Carlsen, T., Schäfer, M., and Wendisch, M.: Airborne measurements of directional reflectivity over the Arctic marginal sea ice zone, *Atmos. Meas. Tech.*, 15, 2939–2953, <https://doi.org/10.5194/amt-15-2939-2022>, 2022.
- Bennartz, R., Shupe, M. D., Turner, D. D., Walden, V. P., Steffen, K., Cox, C. J., Kulie, M. S., Miller, N. B., and Pettersen, C.: July 2012 Greenland melt extent enhanced by low-level liquid clouds, *Nature*, 496, 83–86, <https://doi.org/10.1038/nature12002>, 2013.
- Ceppi, P., Hartmann, D. L., and Webb, M. J.: Mechanisms of the Negative Shortwave Cloud Feedback in Middle to High Latitudes, *J. Clim.*, 29, 139–157, <https://doi.org/10.1175/jcli-d-15-0327.1>, 2015.
- Choi, Y.-S., Hwang, J., Ok, J., Park, D.-S. R., Su, H., Jiang, J. H., Huang, L., and Limpasuvan, T.: Effect of Arctic clouds on the ice-albedo feedback in midsummer, *Int. J. Climatol.*, 40, 4707–4714, <https://doi.org/10.1002/joc.6469>, 2020.
- Cox, C. and Munk, W.: Measurement of the Roughness of the Sea Surface from Photographs of the Sun's Glitter, *J. Opt. Soc. Am.*, 44, 838–850, <https://doi.org/10.1364/josa.44.000838>, 1954.
- Cox, C. J., Walden, V. P., Rowe, P. M., and Shupe, M. D.: Humidity trends imply increased sensitivity to clouds in a warming Arctic, *Nat. Commun.*, 6, <https://doi.org/10.1038/ncomms10117>, 2015.
- Curry, J. A., Schramm, J. L., Rossow, W. B., and Randall, D.: Overview of Arctic Cloud and Radiation Characteristics, *J. Clim.*, 9, 1731–1764, [https://doi.org/10.1175/1520-0442\(1996\)009<1731:OOACAR>2.0.CO;2](https://doi.org/10.1175/1520-0442(1996)009<1731:OOACAR>2.0.CO;2), 1996.
- Dong, X., Xi, B., Crosby, K., Long, C. N., Stone, R. S., and Shupe, M. D.: A 10 year climatology of Arctic cloud fraction and radiative forcing at Barrow, Alaska, *J. Geophys. Res.*, 115, <https://doi.org/10.1029/2009jd013489>, 2010.
- Dupuy, R., Jourdan, O., Mioche, G., Gourbeyre, C., Leroy, D., and Schwarzenböck, A.: CDP, CIP and PIP In-situ arctic cloud microphysical properties observed during ACLOUD-AC3 campaign in June 2017, PANGAEA, <https://doi.org/10.1594/PANGAEA.899074>, 2019.
- Ebell, K., Nomokonova, T., Maturilli, M., and Ritter, C.: Radiative Effect of Clouds at Ny-Ålesund, Svalbard, as Inferred from Ground-Based Remote Sensing Observations, *J. Appl. Meteorol. Climatol.*, 59, 3–22, <https://doi.org/10.1175/jamc-d-19-0080.1>, 2020.
- Ehrlich, A., Stapf, J., Lüpkes, C., Mech, M., Crewell, S., and Wendisch, M.: Meteorological measurements by dropsondes released from POLAR 5 during ACLOUD 2017, PANGAEA, <https://doi.org/10.1594/PANGAEA.900204>, 2019a.
- Ehrlich, A., Wendisch, M., Lüpkes, C., Buschmann, M., Bozem, H., Chechin, D., Clemen, H.-C., Dupuy, R., Eppers, O., Hartmann, J., Herber, A., Jäkel, E., Järvinen, E., Jourdan, O., Kästner, U., Kliesch, L.-L., Köllner, F., Mech, M., Mertes, S., Neuber, R., Ruiz-Donoso, E., Schnaiter, M., Schneider, J., Stapf, J., and Zanatta, M.: A comprehensive in situ and remote sensing data set from the Arc-



- 520 tic CLOUD Observations Using airborne measurements during polar Day (ACLOUD) campaign, *Earth Syst. Sci. Data*, 11, 1853–1881, <https://doi.org/10.5194/essd-11-1853-2019>, 2019b.
- Emde, C., Buras-Schnell, R., Kylling, A., Mayer, B., Gasteiger, J., Hamann, U., Kylling, J., Richter, B., Pause, C., Dowling, T., and Bugliaro, L.: The libRadtran software package for radiative transfer calculations (version 2.0.1), *Geosci. Model Dev.*, 9, 1647–1672, <https://doi.org/10.5194/gmd-9-1647-2016>, 2016.
- 525 Forster, P., Storelvmo, T., Armour, K., Collins, W., Dufresne, J.-L., Frame, D., Lunt, D., Mauritsen, T., Palmer, M., Watanabe, M., Wild, M., and Zhan, H.: The Earth's Energy Budget, Climate Feedbacks, and Climate Sensitivity, in: *Climate Change 2021: The Physical Science Basis. Contribution of Working Group I to the Sixth Assessment Report of the Intergovernmental Panel on Climate Change*, edited by Masson-Delmotte, V., Zhai, P., Pirani, A., Connors, S., Péan, C., Berger, S., Caud, N., Chen, Y., Goldfarb, L., Gomis, M., Huang, M., Leitzell, K., Lonnoy, E., Matthews, J., Maycock, T., Waterfield, T., Yelekçi, O., Yu, R., and Zhou, B., book section 9, pp. 923–1054, Cambridge University Press, Cambridge, United Kingdom and New York, NY, USA, <https://doi.org/10.1017/9781009157896.009>, 2021.
- 530 Gardner, A. S. and Sharp, M. J.: A review of snow and ice albedo and the development of a new physically based broadband albedo parameterization, *J. Geophys. Res.*, 115, <https://doi.org/10.1029/2009jf001444>, 2010.
- Hartmann, J., Lüpkes, C., and Chechin, D.: 1Hz resolution aircraft measurements of wind and temperature during the ACLOUD campaign in 2017, PANGAEA, <https://doi.org/10.1594/PANGAEA.902849>, 2019.
- 535 Hartmann, J., Lüpkes, C., Michaelis, J., and Herber, A.: High resolution aircraft measurements of wind and temperature during the MOSAIC-ACA campaign in 2020, PANGAEA, <https://doi.org/10.1594/PANGAEA.947787>, 2022.
- Intrieri, J. M., Shupe, M. D., Uttal, T., and McCarthy, B. J.: An annual cycle of Arctic cloud characteristics observed by radar and lidar at SHEBA, *J. Geophys. Res.*, 107, <https://doi.org/10.1029/2000jc000423>, 2002.
- Jin, Z., Charlock, T. P., Smith, W. L., and Rutledge, K.: A parameterization of ocean surface albedo, *J. Geophys. Res.*, 31, 26 429–26 443, <https://doi.org/10.1029/2004gl021180>, 2004.
- 540 Jin, Z., Qiao, Y., Wang, Y., Fang, Y., and Yi, W.: A new parameterization of spectral and broadband ocean surface albedo, *Opt. Express*, 19, 26 429–26 443, <https://doi.org/10.1364/oe.19.026429>, 2011.
- Kay, J. E. and L'Ecuyer, T.: Observational constraints on Arctic Ocean clouds and radiative fluxes during the early 21st century, *J. Geophys. Res.: Atmos.*, 118, 7219–7236, <https://doi.org/10.1002/jgrd.50489>, 2013.
- 545 Kay, J. E., Holland, M. M., Bitz, C. M., Blanchard-Wrigglesworth, E., Gettelman, A., Conley, A., and Bailey, D.: The Influence of Local Feedbacks and Northward Heat Transport on the Equilibrium Arctic Climate Response to Increased Greenhouse Gas Forcing, *Journal of Climate*, 25, 5433–5450, <https://doi.org/10.1175/jcli-d-11-00622.1>, 2012.
- Kay, J. E., L'Ecuyer, T., Chepfer, H., Loeb, N., Morrison, A., and Cesana, G.: Recent Advances in Arctic Cloud and Climate Research, *Curr. Clim. Change Rep.*, 2, 159–169, <https://doi.org/10.1007/s40641-016-0051-9>, 2016.
- 550 Konda, M., Imasato, N., Nishi, K., and Toda, T.: Measurement of the sea surface emissivity, *J. Oceanogr.*, 50, 17–30, <https://doi.org/10.1007/bf02233853>, 1994.
- Lüpkes, C., Hartmann, J., Chechin, D., and Michaelis, J.: High resolution aircraft measurements of wind and temperature during the AFLUX campaign in 2019, PANGAEA, <https://doi.org/10.1594/PANGAEA.945844>, 2022.
- Maturilli, M.: High resolution radiosonde measurements from station Ny-Ålesund (2017-04 et seq), PANGAEA, <https://doi.org/10.1594/PANGAEA.914973>, 2020.
- 555 Mech, M., Ehrlich, A., Herber, A., Lüpkes, C., Wendisch, M., Becker, S., Boose, Y., Chechin, D., Crewell, S., Dupuy, R., Gourbeyre, C., Hartmann, J., Jäkel, E., Jourdan, O., Kliesch, L.-L., Klingebiel, M., Kulla, B. S., Mioche, G., Moser, M., Risse, N., Schäfer, M., Stapf, J.,



- and Voigt, C.: MOSAiC-ACA and AFLUX – Arctic airborne campaigns characterizing the exit area of MOSAiC, submitted to Nat. Sci. Data, 2022.
- 560 Miller, N. B., Shupe, M. D., Cox, C. J., Walden, V. P., Turner, D. D., and Steffen, K.: Cloud Radiative Forcing at Summit, Greenland, *Journal of Climate*, 28, 6267–6280, <https://doi.org/10.1175/jcli-d-15-0076.1>, 2015.
- Morrison, A. L., Kay, J. E., Frey, W. R., Chepfer, H., and Guzman, R.: Cloud Response to Arctic Sea Ice Loss and Implications for Future Feedback in the CESM1 Climate Model, *J. Geophys. Res.: Atmos.*, 124, 1003–1020, <https://doi.org/10.1029/2018jd029142>, 2019.
- Moser, M. and Voigt, C.: DLR in-situ cloud measurements during AFLUX Arctic airborne campaign, PANGAEA,
565 <https://doi.org/10.1594/PANGAEA.940564>, 2022.
- Moser, M., Voigt, C., and Hahn, V.: DLR in-situ cloud measurements during MOSAiC-ACA Arctic airborne campaign, PANGAEA, <https://doi.org/10.1594/PANGAEA.940557>, 2022.
- Nixdorf, U., Dethloff, K., Rex, M., Shupe, M., Sommerfeld, A., Perovich, D. K., Nicolaus, M., Heuzé, C., Rabe, B., Loose, B., Damm, E., Gradinger, R., Fong, A., Maslowski, W., Rinke, A., Kwok, R., Spreen, G., Wendisch, M., Herber, A., Hirsekorn, M., Mohaupt, V., Frick-
570 enhaus, S., Immerz, A., Weiss-Tuider, K., König, B., Mengedoh, D., Regnery, J., Gerchow, P., Ransby, D., Krumpfen, T., Morgenstern, A., Haas, C., Kanzow, T., Rack, F. R., Saitzev, V., Sokolov, V., Makarov, A., Schwarze, S., Wunderlich, T., Wurr, K., and Boetius, A.: MOSAiC Extended Acknowledgement, Zenodo, <https://doi.org/10.5281/ZENODO.5541624>, 2021.
- Polavarapu, R. J.: Measurement of Net Radiation from Shipboard Sensors, *J. Appl. Meteorol.* (1962-1982), 17, 1062–1067, <http://www.jstor.org/stable/26178571>, 1978.
- 575 Protat, A., Schulz, E., Rikus, L., Sun, Z., Xiao, Y., and Keywood, M.: Shipborne observations of the radiative effect of Southern Ocean clouds, *J. Geophys. Res.: Atmos.*, 122, 318–328, <https://doi.org/10.1002/2016jd026061>, 2017.
- Ramanathan, V., Cess, R. D., Harrison, E. F., Minnis, P., Barkstrom, B. R., Ahmad, E., and Hartmann, D.: Cloud-Radiative Forcing and Climate: Results from the Earth Radiation Budget Experiment, *Science*, 243, 57–63, <https://doi.org/10.1126/science.243.4887.57>, 1989.
- Schade, N. H., Macke, A., Sandmann, H., and Stick, C.: Enhanced solar global irradiance during cloudy sky conditions, *Meteorol. Z.*, 16,
580 295–303, <https://doi.org/10.1127/0941-2948/2007/0206>, 2007.
- Serreze, M. C. and Barry, R. G.: Processes and impacts of Arctic amplification: A research synthesis, *Global Planet. Change*, 77, 85–96, <https://doi.org/10.1016/j.gloplacha.2011.03.004>, 2011.
- Shupe, M. D. and Intrieri, J. M.: Cloud Radiative Forcing of the Arctic Surface: The Influence of Cloud Properties, Surface Albedo, and Solar Zenith Angle, *J. Clim.*, 17, 616–628, [https://doi.org/10.1175/1520-0442\(2004\)017<0616:crfota>2.0.co;2](https://doi.org/10.1175/1520-0442(2004)017<0616:crfota>2.0.co;2), 2004.
- 585 Shupe, M. D., Rex, M., Blomquist, B., Persson, P. O. G., Schmale, J., Uttal, T., Althausen, D., Angot, H., Archer, S., Bariteau, L., Beck, I., Bilberry, J., Bucci, S., Buck, C., Boyer, M., Brasseur, Z., Brooks, I. M., Calmer, R., Cassano, J., Castro, V., Chu, D., Costa, D., Cox, C. J., Creamean, J., Crewell, S., Dahlke, S., Damm, E., de Boer, G., Deckelmann, H., Dethloff, K., Dütsch, M., Ebell, K., Ehrlich, A., Ellis, J., Engelmann, R., Fong, A. A., Frey, M. M., Gallagher, M. R., Ganzeveld, L., Gradinger, R., Graeser, J., Greenamyre, V., Griesche, H., Griffiths, S., Hamilton, J., Heinemann, G., Helmig, D., Herber, A., Heuzé, C., Hofer, J., Houchens, T., Howard, D., Inoue, J., Jacobi, H.-
590 W., Jaiser, R., Jokinen, T., Jourdan, O., Jozef, G., King, W., Kirchgaessner, A., Klingebiel, M., Krassovski, M., Krumpfen, T., Lampert, A., Landing, W., Laurila, T., Lawrence, D., Lonardi, M., Loose, B., Lüpkes, C., Maahn, M., Macke, A., Maslowski, W., Marsay, C., Maturilli, M., Mech, M., Morris, S., Moser, M., Nicolaus, M., Ortega, P., Osborn, J., Pätzold, F., Perovich, D. K., Petäjä, T., Pilz, C., Pirazzini, R., Posman, K., Powers, H., Pratt, K. A., Preußner, A., Quéléver, L., Radenz, M., Rabe, B., Rinke, A., Sachs, T., Schulz, A., Siebert, H., Silva, T., Solomon, A., Sommerfeld, A., Spreen, G., Stephens, M., Stohl, A., Svensson, G., Uin, J., Viegas, J., Voigt, C., von der Gathen, P.,



- 595 Wehner, B., Welker, J. M., Wendisch, M., Werner, M., Xie, Z., and Yue, F.: Overview of the MOSAiC expedition: Atmosphere, *Elem. Sci. Anth.*, 10, <https://doi.org/10.1525/elementa.2021.00060>, 2022.
- Spreen, G., Kaleschke, L., and Heygster, G.: Sea ice remote sensing using AMSR-E 89-GHz channels, *J. Geophys. Res.*, 113, <https://doi.org/10.1029/2005jc003384>, 2008.
- Stamnes, K., Tsay, S.-C., Wiscombe, W., and Jayaweera, K.: Numerically stable algorithm for discrete-ordinate-method radiative transfer in
600 multiple scattering and emitting layered media, *Appl. Opt.*, 27, 2502–2509, <https://doi.org/10.1364/ao.27.002502>, 1988.
- Stapf, J., Ehrlich, A., Jäkel, E., and Wendisch, M.: Aircraft measurements of broadband irradiance during the ACLOUD campaign in 2017, PANGAEA, <https://doi.org/10.1594/PANGAEA.900442>, 2019.
- Stapf, J., Ehrlich, A., Jäkel, E., Lüpkes, C., and Wendisch, M.: Reassessment of shortwave surface cloud radiative forcing in the Arctic: consideration of surface-albedo–cloud interactions, *Atmos. Chem. Phys.*, 20, 9895–9914, <https://doi.org/10.5194/acp-20-9895-2020>, 2020.
- 605 Stapf, J., Ehrlich, A., and Wendisch, M.: Influence of Thermodynamic State Changes on Surface Cloud Radiative Forcing in the Arctic: A Comparison of Two Approaches Using Data From AFLUX and SHEBA, *J. Geophys. Res.: Atmos.*, 126, <https://doi.org/10.1029/2020jd033589>, 2021a.
- Stapf, J., Ehrlich, A., and Wendisch, M.: Aircraft measurements of broadband irradiance during the AFLUX campaign in 2019, PANGAEA, <https://doi.org/10.1594/PANGAEA.932020>, 2021b.
- 610 Stapf, J., Ehrlich, A., and Wendisch, M.: Cloud radiative forcing, LWP and cloud-free albedo derived from airborne broadband irradiance observations during the AFLUX and ACLOUD campaign, PANGAEA, <https://doi.org/10.1594/PANGAEA.932010>, 2021c.
- Strong, C. and Rigor, I. G.: Arctic marginal ice zone trending wider in summer and narrower in winter, *Geophys. Res. Lett.*, 40, 4864–4868, <https://doi.org/10.1002/grl.50928>, 2013.
- Walsh, J. E. and Chapman, W. L.: Arctic Cloud–Radiation–Temperature Associations in Observational Data and Atmospheric Reanalyses, *J. Clim.*, 11, 3030–3045, [https://doi.org/10.1175/1520-0442\(1998\)011<3030:acrta>2.0.co;2](https://doi.org/10.1175/1520-0442(1998)011<3030:acrta>2.0.co;2), 1998.
- 615 Warren, S. G.: Optical properties of snow, *Rev. Geophys.*, 20, 67–89, <https://doi.org/10.1029/rg020i001p00067>, 1982.
- Wendisch, M., Brückner, M., Burrows, J., Crewell, S., Dethloff, K., Ebell, K., Lüpkes, C., Macke, A., Notholt, J., Quaas, J., Rinke, A., and Tegen, I.: Understanding Causes and Effects of Rapid Warming in the Arctic, *Eos*, 98, <https://doi.org/10.1029/2017eo064803>, 2017.
- Wendisch, M., Macke, A., Ehrlich, A., Lüpkes, C., Mech, M., Chechin, D., Dethloff, K., Velasco, C. B., Bozem, H., Brückner, M., Clemen,
620 H.-C., Crewell, S., Donth, T., Dupuy, R., Ebell, K., Egerer, U., Engelmann, R., Engler, C., Eppers, O., Gehrman, M., Gong, X., Gottschalk, M., Gourbeyre, C., Griesche, H., Hartmann, J., Hartmann, M., Heinold, B., Herber, A., Herrmann, H., Heygster, G., Hoor, P., Jafariserajehlou, S., Jäkel, E., Järvinen, E., Jourdan, O., Kästner, U., Kecorius, S., Knudsen, E. M., Köllner, F., Kretzschmar, J., Lelli, L., Leroy, D., Maturilli, M., Mei, L., Mertes, S., Mioche, G., Neuber, R., Nicolaus, M., Nomokonova, T., Notholt, J., Palm, M., van Pinxteren, M., Quaas, J., Richter, P., Ruiz-Donoso, E., Schäfer, M., Schmieder, K., Schnaiter, M., Schneider, J., Schwarzenböck, A., Seifert, P.,
- 625 Shupe, M. D., Siebert, H., Spreen, G., Stapf, J., Stratmann, F., Vogl, T., Welti, A., Wex, H., Wiedensohler, A., Zanatta, M., and Zeppenfeld, S.: The Arctic Cloud Puzzle: Using ACLOUD/PASCAL Multiplatform Observations to Unravel the Role of Clouds and Aerosol Particles in Arctic Amplification, *Bull. Am. Meteorol. Soc.*, 100, 841–871, <https://doi.org/10.1175/bams-d-18-0072.1>, 2019.
- Wendisch, M., Brückner, M., Crewell, S., Ehrlich, A., Notholt, J., Lüpkes, C., Macke, A., Burrows, J. P., Rinke, A., Quaas, J., Maturilli, M., Schemann, V., Shupe, M. D., Akansu, E. F., Barrientos-Velasco, C., Bärfuss, K., Blechschmidt, A.-M., Block, K., Bougoudis, I.,
630 Bozem, H., Böckmann, C., Bracher, A., Bresson, H., Bretschneider, L., Buschmann, M., Chechin, D. G., Chylik, J., Dahlke, S., Deneke, H., Dethloff, K., Donth, T., Dorn, W., Dupuy, R., Ebell, K., Egerer, U., Engelmann, R., Eppers, O., Gerdes, R., Gierens, R., Gorodetskaya, I. V., Gottschalk, M., Griesche, H., Gryanik, V. M., Handorf, D., Harm-Altstädter, B., Hartmann, J., Hartmann, M., Heinold, B., Herber,



- 635 A., Herrmann, H., Heygster, G., Höschel, I., Hofmann, Z., Hölemann, J., Hünerbein, A., Jafariserajehlou, S., Jäkel, E., Jacobi, C., Janout, M., Jansen, F., Jourdan, O., Jurányi, Z., Kalesse-Los, H., Kanzow, T., Käthner, R., Kliesch, L. L., Klingebiel, M., Knudsen, E. M., Kovács, T., Körtke, W., Krampe, D., Kretzschmar, J., Kreyling, D., Kulla, B., Kunkel, D., Lampert, A., Lauer, M., Lelli, L., von Lerber, A., Linke, O., Löhnert, U., Lonardi, M., Losa, S. N., Losch, M., Maahn, M., Mech, M., Mei, L., Mertes, S., Metzner, E., Mewes, D., Michaelis, J., Mioche, G., Moser, M., Nakoudi, K., Neggers, R., Neuber, R., Nomokonova, T., Oelker, J., Papakonstantinou-Presvelou, I., Pätzold, F., Pefanis, V., Pohl, C., van Pinxteren, M., Radovan, A., Rhein, M., Rex, M., Richter, A., Risse, N., Ritter, C., Rostosky, P., Rozanov, V. V., Donoso, E. R., Saavedra-Garfias, P., Salzmann, M., Schacht, J., Schäfer, M., Schneider, J., Schnierstein, N., Seifert, P., Seo, S., Siebert, 640 H., Soppa, M. A., Spreen, G., Stachlewska, I. S., Stapf, J., Stratmann, F., Tegen, I., Viceto, C., Voigt, C., Vountas, M., Walbröl, A., Walter, M., Wehner, B., Wex, H., Willmes, S., Zanatta, M., and Zeppenfeld, S.: Atmospheric and Surface Processes, and Feedback Mechanisms Determining Arctic Amplification: A Review of First Results and Prospects of the (AC)³ Project, *Bull. Am. Meteorol. Soc.* (published online ahead of print 2022), <https://doi.org/10.1175/bams-d-21-0218.1>, 2022a.
- Wendisch, M., Stapf, J., Becker, S., Ehrlich, A., Jäkel, E., Klingebiel, M., Lüpkes, C., Schäfer, M., and Shupe, M. D.: Effects of variable, 645 ice-ocean surface properties and air mass transformation on the Arctic radiative energy budget, *Atmos. Chem. Phys. Discuss.* (preprint), 2022, 1–31, <https://doi.org/10.5194/acp-2022-614>, 2022b.
- Wesche, C., Steinhage, D., and Nixdorf, U.: Polar aircraft Polar5 and Polar6 operated by the Alfred Wegener Institute, *Journal of Large-scale Research Facilities JLSRF*, 2, <https://doi.org/10.17815/jlsrf-2-153>, 2016.
- Zelinka, M. D., Klein, S. A., and Hartmann, D. L.: Computing and Partitioning Cloud Feedbacks Using Cloud Property Histograms. Part II: 650 Attribution to Changes in Cloud Amount, Altitude, and Optical Depth, *J. Clim.*, 25, 3736–3754, <https://doi.org/10.1175/jcli-d-11-00249.1>, 2012.